ADVANCES IN ATMOSPHERIC SCIENCES, VOL. 26, NO. 2, 2009, 211–221

Comparison of the Bright Band Characteristics Measured by Micro Rain Radar (MRR) at a Mountain and a Coastal Site in South Korea

Joo-Wan CHA[1,2], Ki-Ho CHANG[2], Seong Soo YUM*[1], and Young-Jean CHOI[2]

[1] *Department of Atmospheric Sciences, Yonsei University, Korea*

[2] *Global Environment System Research Laboratory NIMR/KMA, Korea*

(Received 1 November 2007; revised 30 October 2008)

ABSTRACT

Data from a long term measurement of Micro Rain Radar (MRR) at a mountain site (Daegwallyeong, DG, one year period of 2005) and a coastal site (Haenam, HN, three years 2004–2006) in South Korea were analyzed to compare the MRR measured bright band characteristics of stratiform precipitation at the two sites. On average, the bright band was somewhat thicker and the sharpness (average gradient of reflectivity above and below the reflectivity peak) was slightly weaker at DG, compared to those values at HN. The peak reflectivity itself was twice as strong and the relative location of the peak reflectivity within the bright band was higher at HN than at DG. Importantly, the variability of these values was much larger at HN than at DG. The key parameter to cause these differences is suggested to be the difference of the snow particle densities at the two sites, which is related to the degree of riming. Therefore, it is speculated that the cloud microphysical processes at HN may have varied significantly from un-rimed snow growth, producing low density snow particles, to the riming of higher density particles, while snow particle growth at DG was more consistently affected by the riming process, and therefore high density snow particles. Forced uplifting of cloudy air over the mountain area around DG might have resulted in an orographic supercooling effect that led to the enhanced riming of supercooled cloud drops.

Key words: Micro Rain Radar, bright band thickness and sharpness, cloud microphysical processes, local characteristics

Citation: Cha, J.-W., K.-H. Chang, S. S. Yum, and Y.-J. Choi, 2009: Comparison of the bright band characteristics measured by Micro Rain Radar (MRR) at a mountain and a coastal site in South Korea. *Adv. Atmos. Sci.*, **26**(2), 211–221, doi: 10.1007/s00376-009-0211-0.

1. Introduction

A bright band is the enhanced radar echo area that is associated with the melting of hydrometeors in stratiform precipitation. The top of the bright band can be considered as the melting level (or freezing height), commonly accepted as the altitude of the 0°C isotherm (Glickman, 2000). The bright band often leads to an overestimation of precipitation intensity (Rico-Ramirez et al., 2005) and several algorithms have been proposed to correct the effect of the bright band (e.g., Song and Marwitz, 1989; Kitchen et al., 1994; Hardaker et al., 1995; Gray et al., 2002; Neiman et al., 2002).

The characteristics of the bright band may reveal important cloud microphysical processes. Fabry and Zawadzki (1995) reported that the mixture of ice, air, and water leads to a greater increase in the radar reflectivity than that expected from the change from ice to water. They suggest several other factors that contribute to this bright band phenomenon. One such factor is the distribution of water within the particle, so called the density effect. That is, the distribution of melted water within the snow particle will appreciably affect the reflectivity value. Zawadzki et al. (2005) focused more on the density effect and proposed a bright band model, showing that the difference between the peak reflectivity and the snow reflectivity

*Corresponding author: Seong Soo YUM, ssyum@yonsei.ac.kr

increases with a decreasing density of snow particles.

Weather radars such as WSR-88D can be used to detect bright bands by finding the minimum and maximum reflectivity levels (Kitchen et al., 1994). However, time and spatial resolutions are too low for detecting precise bright band information that is required for a detailed cloud microphysics study. Most of the studies on this subject have been conducted using an X-band Doppler radar (e.g., Fabry and Zawadzki, 1995; Drummond et al., 1996; Bellon et al., 1997). Recently, however, Löffler-Mang and Kunz (1999) and Kunhikrishnan et al. (2006) demonstrated that a Micro Rain Radar (MRR), a vertically pointing Doppler radar, could be a very useful instrument to measure the vertical profiles of precipitation and the bright bands, with the advantage of a higher time resolution, a significantly lower cost than X-band radars, and the easiness of operation.

In this study, we present bright band characteristics measured by MRR at the two sites in Korea, one in a mountainous area and the other over a coastal region. Cha et al. (2007) conducted a preliminary study on the MRR measured bright band at this mountain site, following Fabry and Zawadzki's (1995) retrieval algorithm. With the topography induced modifications, the cloud and precipitation developments over the mountainous area are expected to be different from those over a coastal region. Our focus is to elucidate the fundamental differences of the bright band characteristics between the two sites. A literature search indicates that a detailed cloud microphysics study based on the MRR measured bright band characteristics has not been made yet over the northeast Asian region. Long term data presented here also justifies the climatological significance of this study.

2. Data

2.1 *Measurement*

The mountain site is located at the Daegwallyeong Weather Station [hereafter DG, 37°41′N, 128°46′E, 842 m a.s.l. (Above Sea Level)] in the northeastern mountain range of South Korea and the coastal site is located at the Haenam weather observatory (hereafter, HN, 34°33′N, 126°34′E, 14 m a.s.l.) on the southwest coast of South Korea. Supplemental upper air data are obtained from radiosonde measurements at a nearby weather station for each site: Sokcho (hereafter SK, 38°28′N, 128°52′E, 17.6 m a.s.l) is located about 60 km northeast of DG and Kwangju (hereafter KJ, 35°10′N, 126°53′E, 70 m a.s.l.) is about 80 km northeast of HN. Figure 1 shows the four measurement sites.

The MRR data presented in this study are for a

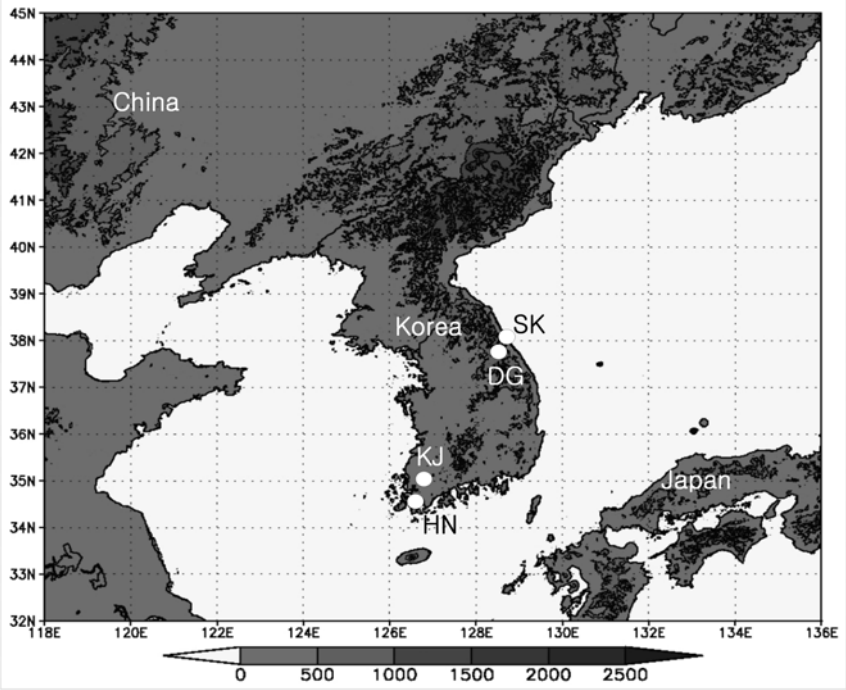

Fig. 1. Map showing the measurement sites; DG: Daegwallyong, mountain MRR site, HN: Haenam, coastal MRR site, SK: Sokcho, upper air observatory near DG, and KJ: Kwangju, upper air observatory near HN. The gray scale represents terrain height (m).

one-year period of 2005 from DG and for three years (2004–2006) from HN. In the analysis of the bright band, we only selected the data that showed a bright band thickness smaller than 1 km to avoid contamination by convective rain. Then, the daily means were calculated to clearly show the relationships between the important parameters, i.e., peak equivalent reflectivity factor (simply "reflectivity" hereafter) in the bright band, top and bottom heights, thickness, and sharpness of the bright band. The MRR cannot clearly identify the transition of snow to rain nor the bright band boundary when the surface temperature is colder than 0°C. Therefore, we limited the MRR data from April to October at each site to avoid these complications, which is similar to Peters and Fisher (2005) approach. On the other hand, the surface and upper air meteorological data were analyzed for all seasons in the three years (2004–2006) at both sites.

2.2 *Instrument*

The Micro Rain radar (MRR) is a vertically pointing FM-CW Doppler radar manufactured by MEteorologische mess TEchniK GmbH (METEK), a German company. The CW-operation makes optimum use of the available transmit power. Thus, a stable and reliable Gunn oscillator with only 50 mW output power can be used for the transmitter. The retrieval of range-resolved Doppler spectra follows the method described by Strauch (1976). The specification of the MRR installed at the two sites is listed in Table 1. In this study, the height resolution of the MRR was 150 m and the time resolution was 1 minute.

Table 1. The specification of the MRR used at DG and HN.

Specification	MRR
Transmit frequency	24 GHz (K-band)
Transmit power	50 mW
Receiver-Transmitter Antenna	offset -parabolic, 0.6 m diameter
Beam Width	1-way, 3 dB
Modulation	FMCW (Frequency modulated continuous wave)
Height resolution	150 m
Averaging time	60 s
Height range	4500 m
Measured variables	Average power spectra of the receiving signal with 2048 lines resolution
Interface	RS232 9600–57600 Baud
Power supply	24 VDC/10 W
Weight	12 kg
Resolution	0.6 m×0.6 m×0.6 m

3. Results

3.1 *Analysis of the upper air and surface weather data*

Before we analyzed the MRR data, we briefly examined the upper air and the surface weather conditions at each site. Since the distance between DG and SK and between HN and KJ is well within the synoptic scale, the upper air data at SK and KJ may represent the vertical weather conditions around DG and HN, respectively. Therefore to avoid complication, the SK upper air data will be designated as DG and KJ as HN in the following discussion.

The Convective Available Potential Energy (CAPE) represents the amount of buoyant energy available to accelerate a parcel vertically, or the amount of work a parcel does on the environment. In Fig. 2a, the monthly average (for the three year period, 2004–2006) of CAPE at HN is larger than that at DG throughout the year and especially more in the summer months. This may suggest that the precipitation at HN may be more convectively driven than that at DG. However, the yearly precipitation is larger at DG (1882 mm) than at HN (1399 mm), mostly due to much greater precipitation at DG in September (Fig. 2b). This huge discrepancy in September precipitation was mainly caused by the heavy precipitation from Typhoon Nabi that hit the eastern part of Korea in September 2005. However, even discarding this abnormal month, the precipitation at DG is still somewhat larger than that at HN, maybe due to the orographic enhancement of precipitation in the mountainous region around DG. Many mountain meteorologists have long recognized that when a moist layer of air rises over a mountain barrier, precipitation amounts increase sharply with the distance up the slope to a certain elevation (Hill, 1881; Hann, 1902; Henry, 1902; Reed and Kincer, 1917; Henry, 1919; Peck and Brown, 1962; Frei and Schaer, 1998). The yearly average temperature at HN (13.5°C) is almost 7°C higher than that at DG (6.6°C), obviously due to the altitude and latitude differences of the two sites. In particular, the monthly average temperature at DG in January, February, March, November, and December is below 0°C (Fig. 2b). This is the reason why we selected the MRR data only from April to October in this study.

The most frequently appearing cloud type is stratocumulus (Sc) both at DG and HN (Fig. 3). For the bright band phenomena, stratiform clouds [i.e., stratus (St), nimbostratus (Ns), and altostratus (As)] are more important. Figure 3 indicates that DG has somewhat of a higher tendency to have these stratiform cloud types while HN more often has the cumuliform cloud types (Ac, Sc, and Cu), which is consistent with

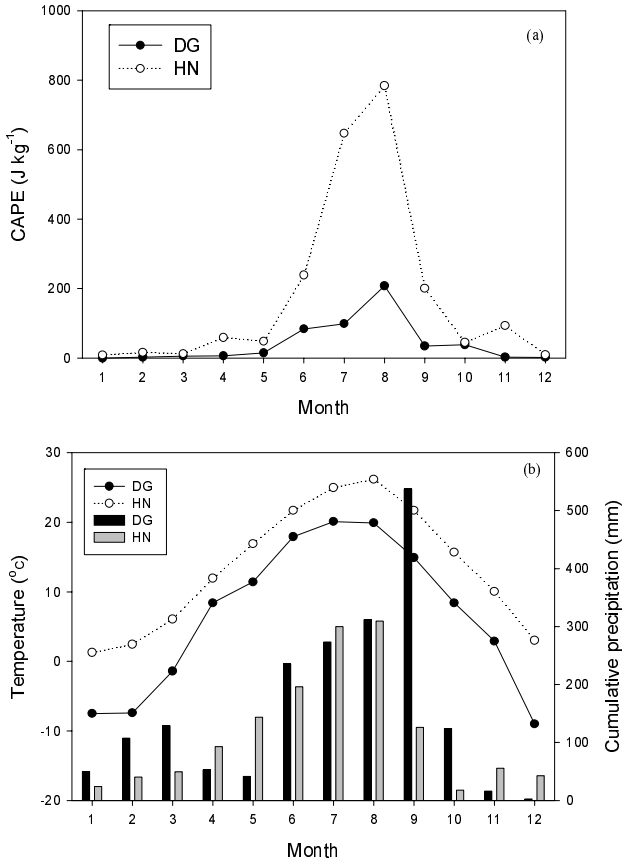

Fig. 2. Variations of monthly mean (a) CAPE (J kg^{-1}), and (b) cumulative precipitation (bars) and the surface temperature (open- and closed-circle line) for the three year period of 2004–2006 at DG and HN.

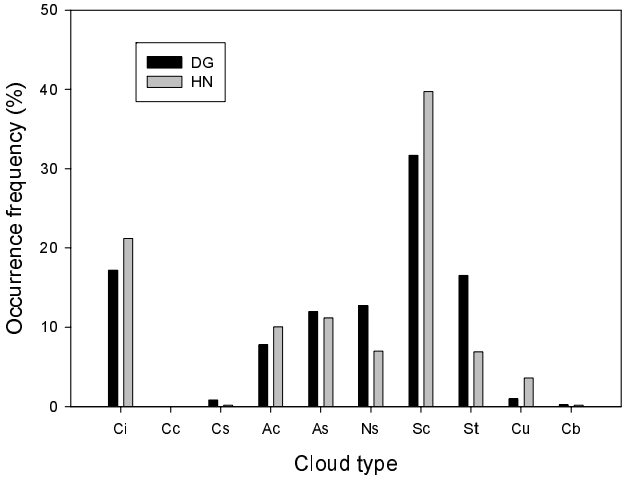

Fig. 3. Occurrence frequency of different cloud types for the three year period of 2004–2006 at DG and HN. The cloud type names follow the WMO convention.

a larger CAPE at HN (Fig. 2a).

3.2 *Classification of MRR precipitation reflectivity types*

Fabry and Zawadzki (1995) grouped the various vertical reflectivity profiles measured by an X-band radar into five classes. The 15-m height resolution was good enough to appropriately classify the reflectivity types into five classes in their results, but this was not the case in our MRR data of the 150 m resolution. Instead, we classified the reflectivity profiles into three classes, using similar criteria employed by Fabry and Zawadzki (1995).

(1) Low level rain (Type 1)

This type includes no ice phase precipitation particles where the echo top is usually lower than the level of the 0°C isotherm, recognized by the radiosonde profile. Precipitating fog and generally a low level stratiform rain, forming only in the liquid form, are the types of precipitation producing a Type 1 profile.

(2) Rain with a bright band (Type 2)

This type is the most common stratiform precipitation profile that shows a bright band. The vertical reflectivity profile is almost constant from the surface up to the bottom of the bright band. The reflectivity of snow usually decreases for the first kilometer above the top of the bright band. Fabry and Zawadzki (1995) designated separate types for rain with a bright band and compact ice, but this was not possible in our MRR data because of a low spatial resolution and they both must have been classified into Type 2.

(3) Convective rain (Type 3)

This type includes rain showers and deep convective rains. The rain shower usually comes in two forms, isolated showers or convective rain bands, with the echo tops generally being between the −5°C and +5°C isotherms. The reflectivity is generally constant from the ground up to 1 km above the echo peak, beyond which the reflectivity rapidly decreases. A deep convective rain displays a dramatic variability of reflectivity in time. Most of the cases with a relatively strong reflectivity extend several kilometers above the 0°C isotherm.

Table 2 summarizes the frequency of occurrence

Table 2. Classification of the MRR precipitation reflectivity profiles at DG in 2005 and at HN from 2004 to 2006.

	Type 1 Low level rain	Type 2 Rain with bright band	Type 3 Convective rain
DG (%)	37	49	14
HN (%)	12	37	51

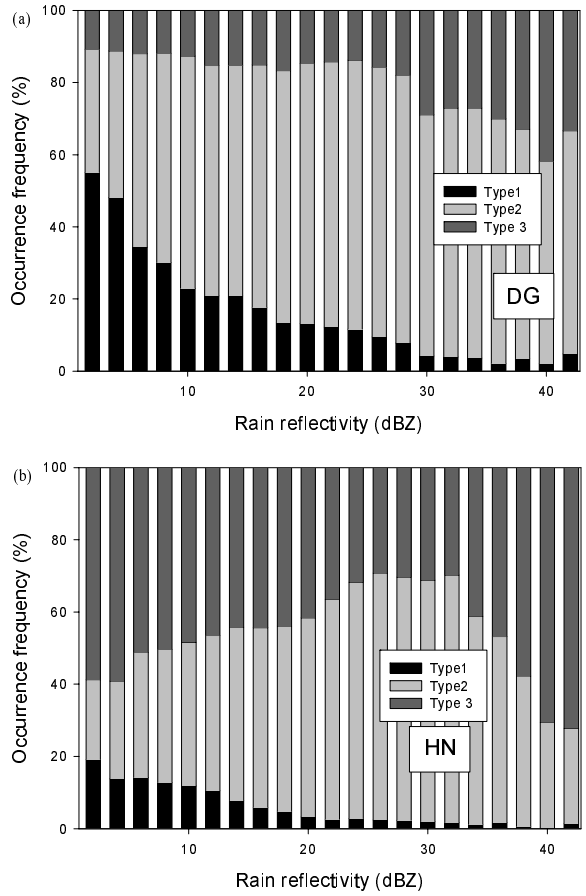

Fig. 4. Occurrence frequency of the three types of precipitation reflectivity profiles as a function of the rain reflectivity near the surface (a) at DG in 2005 and (b) at HN in 2004–2006.

of the three MRR precipitation types at the two sites. Type 2 was observed with the highest frequency at DG but it was Type 3 that appeared with the highest frequency at HN, consistent with the larger CAPE (Fig. 2a). Of note, is the relative high frequency of low level rain events (Type 1) at DG; the orographic enhancement effect might have successfully induced precipitation from otherwise non-precipitating clouds.

Figure 4 shows the frequency of occurrence of the three MRR precipitation types as a function of reflectivity. At DG (Fig. 4a), Type 1 is more frequently observed when the reflectivity is smaller and the opposite is the case for Type 3, which would be expected considering the nature of the precipitation types they represent. However, the most dominant is the Type 2 for all reflectivity values, including the highest reflectivity, indicating that stratiform rain can be heavy at DG. A unique distribution is shown at HN (Fig. 4b): even at very small reflectivity values, Type 3 was the most dominantly observed, but Type 2 is dominant in the mid range of reflectivity and then Type 3 becomes dominant again at higher reflectivities. There were relatively more occurrences of Type 1 events at DG than at HN for higher reflectivities (say, >30 dBZ), maybe due to the orographic enhancement effect at DG, such as the seeder-feeder mechanism and the forcing of precipitation by upslope flow (Browning, 1990). To note, is the bright band characteristics of the Type 2 precipitation reflectivity are discussed hereafter.

3.3 *Retrieval and analysis of the bright band*

A flowchart briefly describing our bright band detection algorithm is shown in Fig. 5. The definitions of the important parameters that can be retrieved with the algorithm are explained in Fig. 5, following the studies of Klaassen (1988) and Fabry and Zawadzki (1995). Newly added in this study is the bright band sharpness (defined later).

The height of the peak reflectivity ($Z_{\mathrm{e(peak)}}$) in the bright band is H_{peak}. The bright band top height (H_{T}) is determined as the altitude that showed the largest negative gradient of Z_{e}. A similar criterion is used to find the bright band bottom height (H_{B}); the altitude of the largest positive gradient of Z_{e}. This is different from the bright band detection method usually used for X-band Doppler radars, i.e., the SNR (Signal and Noise Ratio), falling velocity, and reflectivity (White et al., 2002). In Fig. 6, the reflectivity of snow [$Z_{\mathrm{e(snow)}}$] and rain [$Z_{\mathrm{e(rain)}}$] are defined as the Z_{e} at 150 m above H_{T} and below H_{B}, respectively. The bright band thickness ($\mathrm{BB_{th}}$) is simply $H_{\mathrm{T}} - H_{\mathrm{B}}$. The relative peak position (R_{peak}) in the bright band is defined as,

$$R_{\mathrm{peak}} = \frac{H_{\mathrm{peak}} - H_{\mathrm{B}}}{\mathrm{BB_{th}}}. \tag{1}$$

The bright band sharpness ($\mathrm{BB_{sh}}$) is an average measure of the reflectivity gradient within the bright band and is calculated as follows,

$$\mathrm{BB_{sh}} = \frac{\Delta Z}{\mathrm{BB_{th}}}\,, \tag{2}$$

where ΔZ=[($Z_{\mathrm{e(peak)}}/Z_{\mathrm{e(rain)}}$)+($Z_{\mathrm{e(peak)}}/Z_{\mathrm{e(snow)}}$)]/2.

Figure 7 shows the relationships between the H_{T} derived from the MRR data and the freezing height (H_{f}) measured by the radiosonde. To note is that only the cases when both the MRR and the radiosonde data are available at the same time are included in Fig. 7 and therefore the number of data points in Fig. 7 is not the same as those in the ensuing discussion. The averages of H_{T} and H_{f} in Fig. 7 are close to each other: 4019 m and 4042 m, respectively, at DG and 3365 m and 3236 m at HN. Notably, these values are significantly larger at DG than at HN and the range of these values are much wider at HN, the reason of

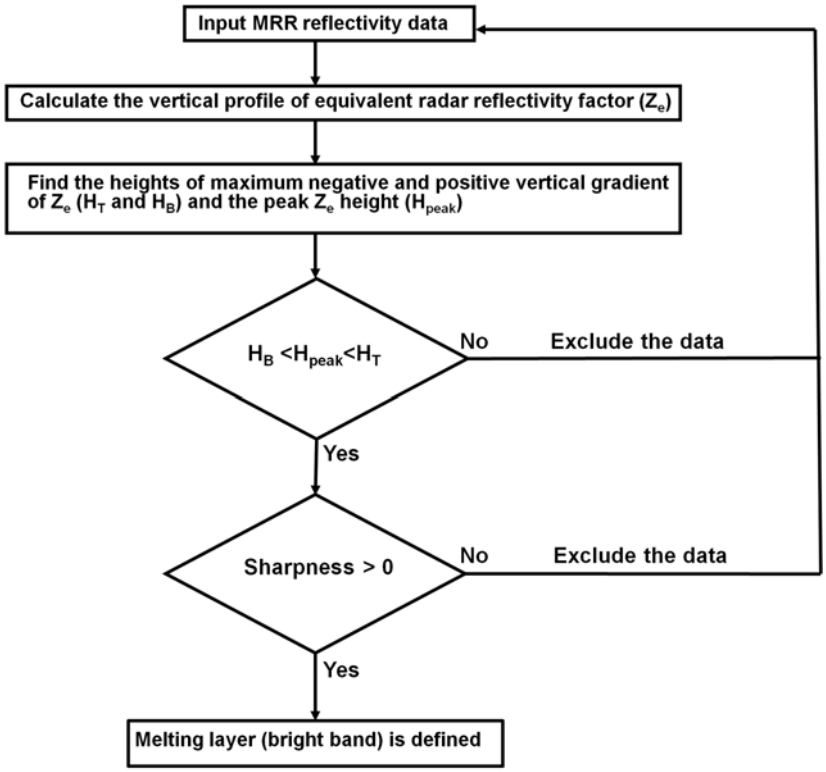

Fig. 5. Flowchart describing the method used to deduce the bright band.

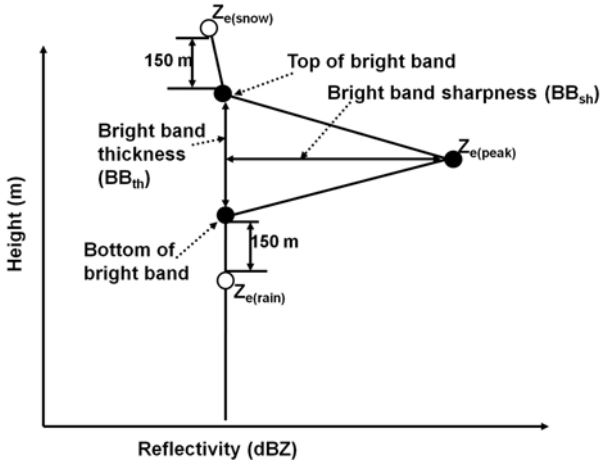

Fig. 6. Schematic drawing that illustrates the various parameters extracted from the MRR reflectivity data.

which is not immediately known. The RMSE values of 329 m (DG) and 367 m (HN) are relatively small, considering that the vertical resolution is 150 m for the MRR data. The measurement range of the MRR is 4500 m. Therefore, if the H_T exceeds 4500 m plus the site altitude, which amounts to 5342 m at DG and 4513 m at HN, this cannot be properly identified from the MRR measurement. No wonder the H_T values in Fig. 7 are limited to this value for each site. Nevertheless, the correspondence is convincingly good and suggests that the H_T from the MRR data can be used as a good estimate of the freezing height.

The frequency of occurrence of BB_{th}, and BB_{sh} are shown in Fig. 8. The BB_{th} at DG is mostly concentrated in between 500 m and 600 m, but the BB_{th} at HN is more evenly distributed in a wider range with the highest frequency at 600 m (Fig. 8a). The highest frequency of occurrence of BB_{sh} is shown at around 3 dB km^{-1} at both DG and HN, with a large tail on the right side. It is not uncommon, however, to find BB_{sh} greater than 6 dB km^{-1} at HN (Fig. 8b). Figure 8 shows that BB_{th} and BB_{sh} are more widely varied at HN than at DG. The thickness and sharpness of a bright band would be highly dependent on snow particle characteristics, such as the melting rate, fall velocity, shape of the snow particles, condensation, evaporation, and aggregation/breakup. However, the two most important factors would be the melting rate and the falling velocity, as Wexler (1955) and Fabry and Zawadzki (1995) reported that those two factors contribute about 80% of the reflectivity change in the bright band. The melting rate is determined by the distribution of water within the snow particles, which also determines the density of the snow particles. Fall velocity is also closely related to the density. Zawadzki et al. (2005) described this as the density effect and

would be most important in stratiform precipitation where the snow particles are large and their density is low (Fabry and Zawadzki, 1995). If snow particles are denser, the BB_{th} would be larger since they would fall faster, but the peak reflectivity would be less pronounced because of a relatively smaller difference from the raindrop density, and therefore a smaller BB_{sh} would be expected. Since the riming of supercooled droplets increases the snow particle density (Rogers and Yau, 1989), the tendency of the larger BB_{th} and the smaller BB_{sh} at DG would be indicative of a greater degree of riming at DG than at HN.

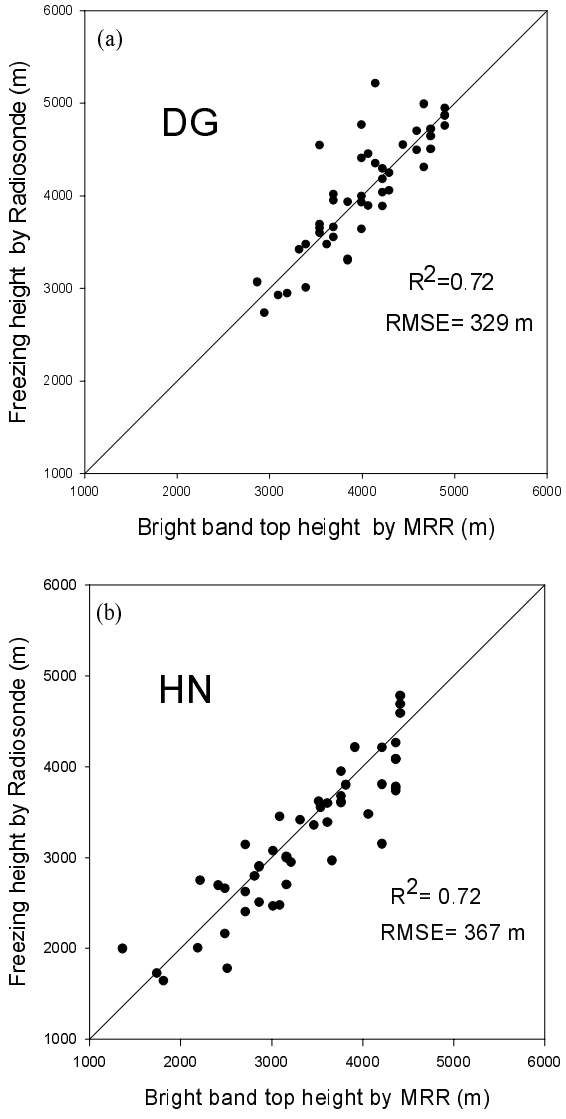

Fig. 7. Comparison of the bright band top height (H_T) derived from the MRR data with the freezing height (H_f) measured by the radiosonde during April–October (a) at DG in 2005 and (b) at HN in 2004–2006. As noted in the text, the radiosonde data of DG (or HN) are actually from SK (or KJ).

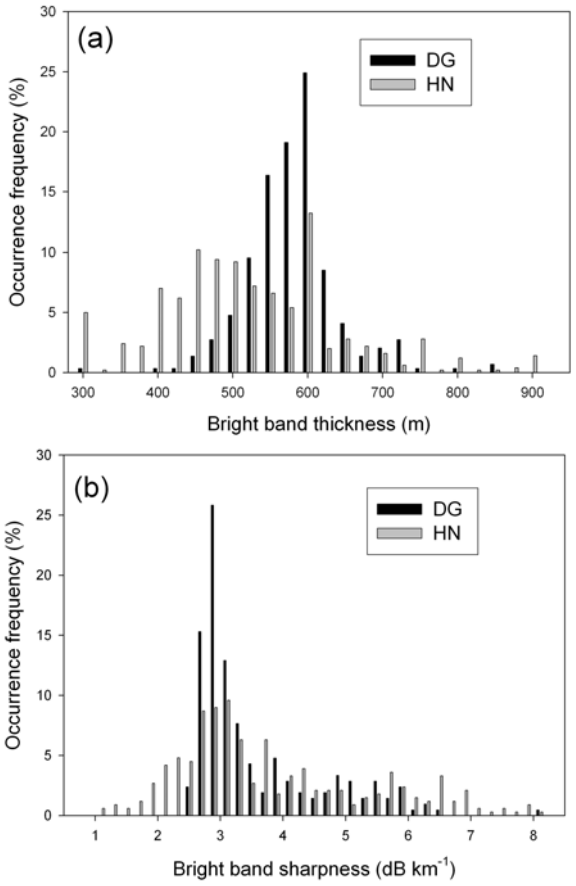

Fig. 8. Occurrence frequency of the bright band (a) thickness (BB_{th}) and (b) sharpness (BB_{sh}) with the Type 2 reflectivity profiles measured during April–October in 2005 (at DG) and in 2004–2006 (at HN).

A scatterplot of $Z_{e(peak)}$ vs. $Z_{e(rain)}$ and of $Z_{e(snow)}$ vs. $Z_{e(rain)}$ is shown in Fig. 9. The very good linear relationships between these parameters for both sites are consistent with the general bright band assumption that aggregation and breakup can be neglected in the bright band model. That is, one snow particle converts to one raindrop (Thurai and Hanado, 2004; Zawadzki et al., 2005). Based on these results, a bright band parameterization can be proposed. At DG,

$$Z_{e(peak)} = 1.742 + 1.193 Z_{e(rain)}, \quad (3)$$

$$Z_{e(snow)} = -0.8 + 0.73 Z_{e(rain)}. \quad (4)$$

At HN,

$$Z_{e(peak)} = 1.773 + 1.138 Z_{e(rain)}\ , \quad (5)$$

$$Z_{e(snow)} = -0.41 + 0.56 Z_{e(rain)}\ . \quad (6)$$

As expected from Eq. (2), BB_{sh} shows a great linear relationship with the ratio of $Z_{e(peak)}/Z_{e(rain)}$ or

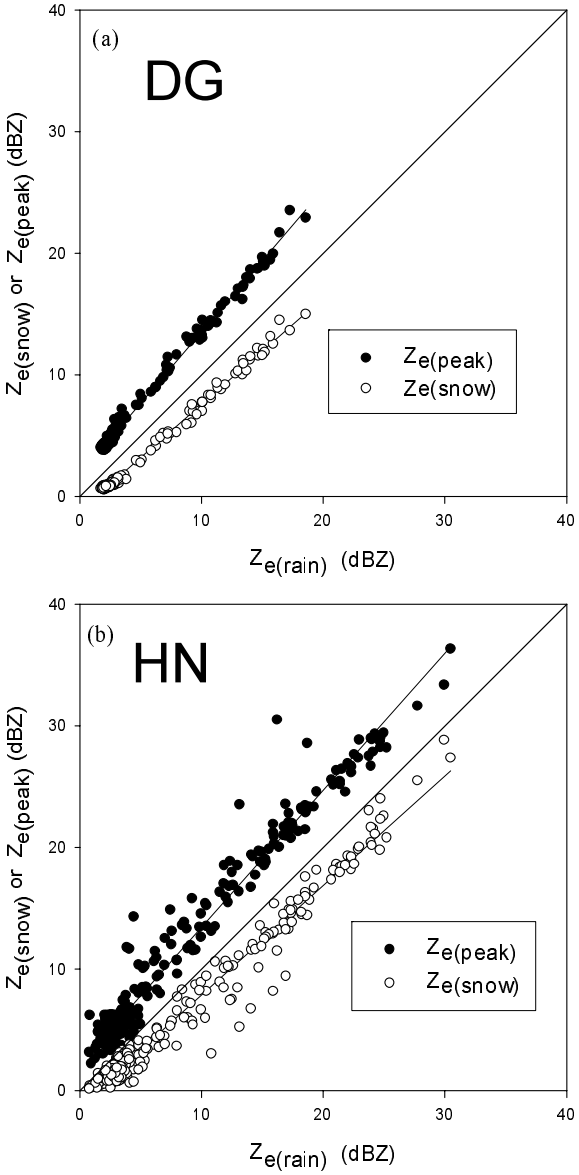

Fig. 9. Scatterplot of the rain reflectivity [$Z_{e(rain)}$] vs. the snow [$Z_{e(snow)}$] or the peak [$Z_{e(peak)}$] reflectivity (a) at DG and (b) at HN. The measurement period is from April to October in 2005 at DG and in 2004–2006 at HN. The one to one line is also shown.

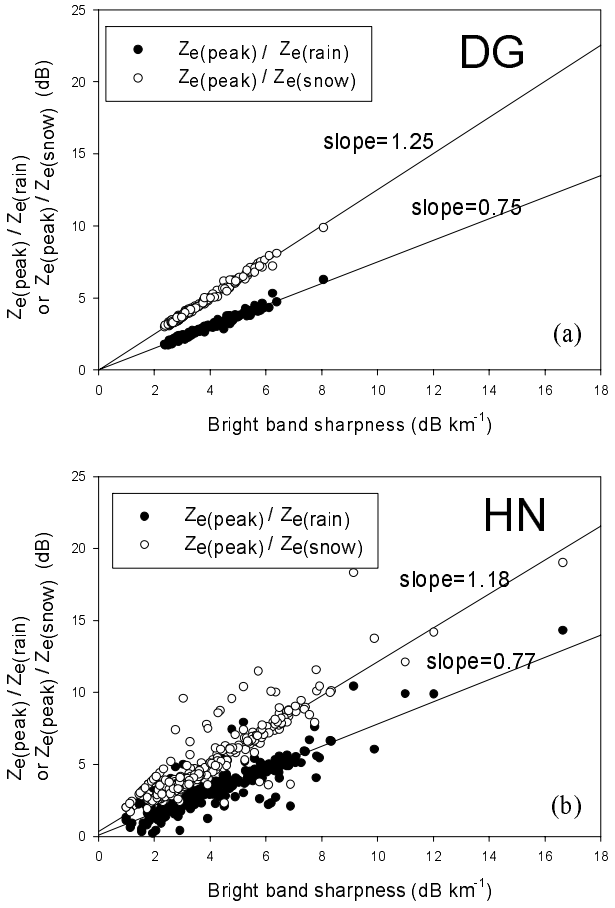

Fig. 10. Same as Fig. 9 except the daily mean bright band sharpness (BB_{sh}) vs. the ratio of $Z_{e(peak)}/Z_{e(rain)}$ or $Z_{e(peak)}/Z_{e(snow)}$ (a) at DG and (b) at HN.

$Z_{e(peak)}/Z_{e(snow)}$ at both sites (Figs. 10a and 10b). The slope for $Z_{e(peak)}/Z_{e(snow)}$ is larger than that for $Z_{e(peak)}/Z_{e(rain)}$ at both sites, due to the density variation of snow particles as opposed to the constancy of the raindrop density (Fabry and Zawadzki, 1995). The important point would be that the data points for $Z_{e(peak)}/Z_{e(snow)}$ are scattered in a greater range at HN than at DG. The $Z_{e(peak)}/Z_{e(snow)}$ ratio would be larger when the snow particle density is smaller (Zawadzki et al., 2005). The greater range of $Z_{e(peak)}/Z_{e(snow)}$ values at HN would suggest a greater

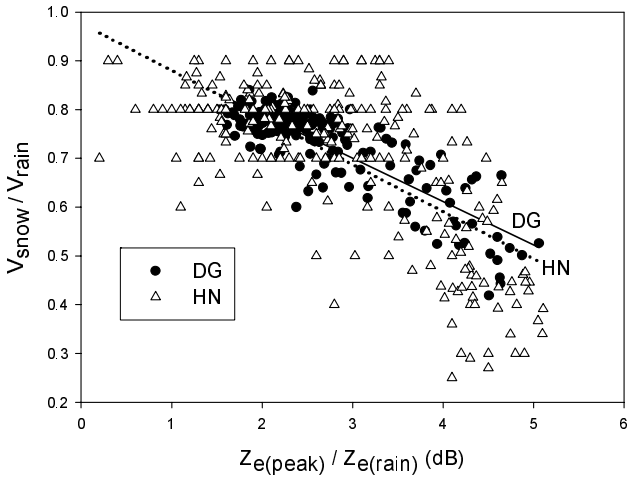

Fig. 11. Relationship between the ratio of the peak-to-rain reflectivity [$Z_{e(peak)}/Z_{e(rain)}$] and the ratio of the snow-to-rain velocity (V_{snow}/V_{rain}) from the MRR reflectivity measurement during April–October in 2005 at DG and in 2004–2006 at HN.

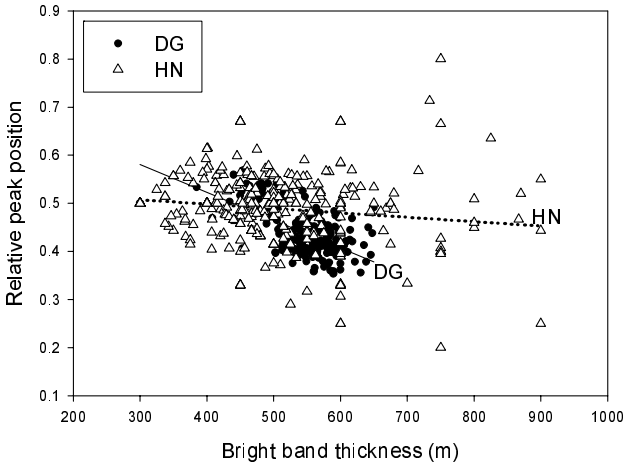

Fig. 12. Same as Fig. 11 except between the bright band thickness (BB_{th}) and the relative peak position (R_{peak}).

variation of snow density at HN. On the other hand, the $Z_{e(peak)}/Z_{e(snow)}$ being confined to relatively smaller values at DG, might indicate a greater degree of riming that would increase the snow density.

When the rain intensity was strong (i.e., MRR peak reflectivity is strong), the estimation of V_{snow} from the MRR data was problematic due to severe attenuation and V_{snow} was calculated to be larger than V_{rain} in many cases. These cases were discarded and it confined $Z_{e(peak)}$ $/Z_{e(rain)}$ to a small value in Fig. 11, where the maximum $Z_{e(peak)}/Z_{e(rain)}$ value barely exceeds 5 dB. Nevertheless, the V_{snow}/V_{rain} ratio shows a tendency to decrease as $Z_{e(peak)}/Z_{e(rain)}$ increases at both sites as expected, and the magnitude of the slope of the relationship is slightly larger at HN than at DG, which is another indication of a greater snow density at DG. If the cases with larger $Z_{e(peak)}$ $/Z_{e(rain)}$ were properly estimated, we may see more obvious differences of the $Z_{e(peak)}$ $/Z_{e(rain)}$ vs. V_{snow}/V_{rain} relationship between DG and HN.

Figure 12 presents the relationship between BB_{th} and R_{peak} [Eq. (1)]. The relative position of the peak within the bright band may reveal important information of the hydrometeors in the bright band. If the snow particles have a low density, they would fall slowly while the melting over the surface would occur more rapidly. As the melting proceeds, their falling speed would gradually increase and this speed should be much faster than when they first began to fall into the bright band as snow particles. The same can be said for snow particles with a high density such as rimed particles, but the relative difference of the fall speed before and after the melting would be relatively small. This suggests that R_{peak} should be large (i.e., close to H_T) when the snow density is low and vice versa. As discussed above, BB_{th} is expected to be smaller when the snow density is lower. This would predict a negative relationship between BB_{th} and R_{peak}. This is the case for DG but HN does not show any tendency in Fig. 12. However, it is obvious that the majority of the data points for HN is to the left and above of the DG data points, confirmed by the average values in Table 3 (discussed immediately).

Table 3 summarizes the average statistics of the bright band characteristics. Unlike Fig. 7, the average H_T for the entire dataset is slightly larger at HN than at DG but the variability is much larger at HN.

The same is true for H_B. This reflects the latitudinal difference of the two sites, i.e., DG being located further north and therefore colder. The average BB_{th} is about 10% larger at DG than at HN while the opposite is true for the average BB_{sh}. Again, the variability of these values is much larger at HN. The average $Z_{e(peak)}$ is twice as large at HN. Finally, the smaller R_{peak} at DG (Fig. 12) is confirmed in Table 3. Collectively, these results suggest that the cloud microphysical processes at HN may have varied significantly from un-rimed snow growth, producing low density snow particles, to the riming of higher density particles, while the riming process seemed to occur more consistently at DG, and therefore higher density snow particles.

4. Conclusion

A long term measurement of MRR at the two sites in Korea, representing a mountain region (Daegwallyeong, DG, one year period of 2005) and a coastal region (Haenam, HN, three years 2004–2006) were analyzed to find the microphysical differences of the precipitating clouds at the two sites. Stratiform precipitation was more prevalent at the mountain site, DG, but convective precipitation tended to occur more at

Table 3. Averages of the bright band characteristics, top height (H_T), bottom height (H_B), thickness (BB_{th}), sharpness (BB_{sh}), peak reflectivity [$Z_{e(peak)}$], and relative peak position (R_{peak}) for the Type 2 reflectivity profiles measured during April–October in 2005 (at DG) and in 2004–2006 (at HN).

	H_T (m)	H_B (m)	BB_{th} (m)	BB_{sh} (dB km^{-1})	$Z_{e(peak)}$ (dBZ)	R_{peak}
DG	3398±299	2850±319	548±49	3.46±1.03	7.52±4.8	0.44±0.04
HN	3676±816	3176±852	500±114	3.87±1.86	15.99±7.9	0.52±0.07

the coastal site, HN.

Focus was given to the stratiform precipitation patterns that usually showed a distinct bright band feature. To avoid the complicated situation of the surface being colder than 0°C, the data only from warmer months (April-October) were selected for analysis. On average, the bright band was somewhat thicker and the sharpness (average gradient of reflectivity above and below the reflectivity peak) was slightly weaker at DG, compared to those values at HN. The peak reflectivity itself was twice as strong and the relative location of the peak reflectivity within the bright band was higher at HN than at DG. Importantly, the variability of these values was much larger at HN than at DG. The key parameter to cause these differences is suggested to be the difference of the snow particle densities at the two sites, which is related to the degree of riming (Zawadzki et al., 2005). Based on these results, we may further suggest that the cloud microphysical processes at HN may have varied significantly from un-rimed snow growth, producing low density snow particles, to the riming of higher density particles, while snow particle growth at DG was more consistently affected by the riming process, and therefore high density snow particles. Forced uplifting of cloudy air over the mountain area around DG might have resulted in an orographic supercooling effect that led to the enhanced riming of supercooled cloud drops (White et al., 2002).

This study demonstrated the potential of MRR as an instrument that may reveal important cloud microphysical characteristics of the bright band. The good correspondence of the MRR that retrieved the bright band top height and the freezing height from radiosonde measurements (Fig. 7), suggests that the MRR can also provide a reliable and continuous estimate of the freezing height. Relatively cheap cost and the easiness of operation promote the attractiveness of the instrument. An immediate application can be found in the business of cloud seeding, where continuous monitoring of the vertical structures of the thermodynamic and cloud microphysical properties is crucial to determine proper seeding location and time.

However, many uncertainties remain in understanding the cloud microphysical characteristics of the MRR reflectivity and the bright band, which requires more elaborate efforts from the research community. In this regard, modeling studies of stratiform cloud and precipitation development may need to be combined with the measurement analysis. As discussed, the MRR is subject to severe attenuation when the rain intensity is high and this limits the reliability of the instrument to relatively weak precipitation events. Finding a way to overcome this limitation will be the task for enhancing the applicability of MRR.

Acknowledgements. This work was funded by the Korean Meteorological Administration Research and Development Program under Grant CATER 2006-2307. The authors are grateful to the National Institute of Meteorological Research (NIMR) for providing the MRR and other meteorological data.

REFERENCES

Bellon, A., I. Zawadzki, and F. Fabry, 1997: Measurements of melting layer attenuation at X-band frequencies. *Radio Science*, **32**, 943–955.

Browning, K. A., 1990: Organization and internal structure of synoptic and mesoscale precipitation system in midlatitudes. *Radar in Meteorology*, D. Atlas, Ed., Amer. Meteor. Soc., 433–460.

Cha, J. W., S. S. Yum, K. H. Chang, and S. N. Oh, 2007: Estimation of the melting layer from a Micro Rain Radar (MRR) data at the Cloud Physics Observation System (CPOS) site at Daegwallyeong Weather Station. *J. Korean Meteor. Soc.*, **43**, 77–85.

Drummond, F. J., R. R. Rogers, S. A. Cohn, W. L. Eckiund, D. A. Cater, and J. S. Wilson, 1996: A new look at the melting layer. *J. Atmos. Sci.*, **53**, 759–769.

Fabry, F., and I. Zawadzki, 1995: Long-term radar observation of the melting layer of precipitation and their interpretation. *J. Atmos. Sci.*, **52**, 838–851.

Frei, C., and C. Schaer, 1998: A precipitation climatology of the Alps from high-resolution rain gage observations. *International Journal of Climatology*, **18**, 873–900.

Glickman, T. S., 2000: *Glossary of Meteorology.* 2d Ed. Amer. Meteor. Soc., 855pp.

Gray, W. R., M. J. Uddstrom, and H. R. Larsen, 2002: Radar surface rainfall estimates using a typical shape function approach to correct for the variation in the vertical profile of reflectivity factor. *Int. J. Remote Sens.*, **23**, 2489–2504.

Hann, J., 1902: Increase of rainfall with altitude. *Mon. Wea. Rev.*, **30**, 218–220.

Hardaker P. J., A. R. Holt, and C. G. Collier, 1995: A melting layer model and its use in correcting for the bright band in single polarization radar echoes. *Quart. J. Roy. Meteor. Soc.*, **121**, 495–525.

Henry, A. J., 1902: Average annual precipitation in the Unites States for the period 1871 to 1901. *Mon. Wea. Rev.*, **30**, 207–213.

Henry, A. J., 1919: Increase of precipitation with altitude. *Mon. Wea. Rev.*, **47**, 33–41.

Hill, S. A., 1881: The meteorology of the North-West Himalaya. Memoris, Vol. 1, India Meteor. Dept., 377–426.

Kitchen, M., R. Brown, and A. G. Davies, 1994: Real time correction of weather radar data for the effects of bright band, range and orographic growth in the widespread precipitation. *Quart. J. Roy. Meteor. Soc.*, **120**, 1231–1254.

Klaassen, W., 1988: Radar observations and simulations of the melting layer of precipitation. *J. Atmos. Sci.*, **45**, 3741–3753.

Kunhikrishnan, P. K., B. R. Sivaraman, N. V. P. Kiran Kumar, and D. P. Alappattu, 2006: Rain observations with micro rain radar (MRR) over Thumba. *Optical Engineering*, **6408**, doi: 10.1117/12.694115.

Löffler-Mang, M., and M. Kunz, 1999: On the performance of a low-cost K-band Doppler radar for quantities rain measurements. *J. Atmos. Oceanic Technol.*, **16**, 379–387.

Neiman, P. J., M. Ralph, A. B. White, D. A. Kingsmill, and P. O. G. Persson, 2002: The statistical relationship between upslope flow and rainfall in California's coastal mountains: Observations during CALJET. *Mon. Wea. Rev.*, **130**, 1468–1492.

Peck, E. L., and M. J. Brown, 1962: An approach to the development of isotheral maps for mountainous areas. *J. Geophys. Res.*, **67**, 681–694.

Peters, G., and B. Fischer, 2005: Profiles of raindrop size distribution as retrieved by Micro rain Radars. *J. Appl. Meteor.*, **44**, 1930–1949.

Reed, W. G., and J. B. Kincer, 1917: The preparation of precipitation charts. *Mon. Wea. Rev.*, **45**, 233–235.

Rico-Ramirez, M. A., I. D. Cluckie, and D. Han, 2005: Correction of the bright band using dual-polarization radar. *Atmospheric Science Letters*, **6**, 40–46.

Rogers, R. R., and M. K. Yau, 1989: *A Short Course in Cloud Physics*. 3d ed., Pergamon Press, 293pp.

Song, N., and J. Marwitz, 1989: A numerical study of the warm rain process in orographic cloud. *J. Atmos. Sci.*, **46**, 3479–3489.

Strauch, R. G., 1976: Theory and application of the FM-CW Doppler radar. Ph. D. dissertation, Electrical Engineering, University of Colorado, 97pp.

Thurai, M., and H. Hanado, 2004: Melting layer model evaluation using fall velocity. *IEE Proc. Microw. Antennas Propag.*, **151**, 465–472.

Zawadzki, I., W. Szyrmer, C. Bell, and F. Fabry, 2005: Modeling of the melting layer. Part III: The density effect. *J. Atmos. Sci.*, **62**, 3705–3723.

Wexler, R., 1955: An evaluation of the physical effects in the melting layer. Preprints, *Fifth Weather Radar Conf.*, Fort Monmouth, NJ, Amer. Meteo. Soc., 329–334.

White, A. B., and D. J. Gottas, E. T. Strem, F. M. Ralph, and P. J. Neiman, 2002: An automated bright band height detection algorithm for use with Doppler radar spectral moment. *J. Atmos. Oceanic Technol.*, **19**, 687–697.